SUPPORTING INFORMATION

Atomistic Mechanisms of Guanidinium Chloride Passivation for Suppressing Ion Migration and Environmental Degradation in $MAPbI_3$ and $FAPbI_3$ Perovskites

Annafi Ado Yaro[1], Waranchit Ruengsrisang[2], Non Thongprong[1*],

[1]*Nanoscience and Nanotechnology Graduate Program, Faculty of Science, King Mongkut's University of Technology Thonburi, 126 Pracha-Uthid Road, Bang Mot, Thung-Khru, Bangkok 10140, Thailand*

[2]*Department of Physics, Faculty of Science, King Mongkut's University of Technology Thonburi, 126 Pracha-Uthid Road, Bang Mot, Thung-Khru, Bangkok 10140, Thailand*

[*]Corresponding author: non.tho@kmutt.ac.th

COMPUTATIONAL METHODS:

The Density Functional Theory (DFT) simulations were performed using the Quantum ESPRESSO simulation package (version 6.7) utilizing the Generalized Gradient Approximation (GGA).[1,2]The study employed the Projected Augmented Wave (PAW) pseudopotential in conjunction with the Perdew–Burke–Ernzerhof (PBE) exchange–correlation functional to accurately describe the interaction between ions and electrons as well as the exchange–correlation effects. [3] Long-range dispersion interactions were accounted for using the semi-empirical Grimme DFT-D3 van der Waals correction scheme.[4] An energy cut-off of 60 eV for the wave function and 540 eV for the charge density was used for the plane-wave expansion. The total energy convergence criteria were set to 10^{-5} eV and 10^{-6} eV for geometric optimization and self-consistent field (SCF) cycles, respectively. During geometric optimization, the atomic Hellmann–Feynman force convergence threshold was set to 0.005 Ry/Å. The reciprocal space was sampled using the Monkhorst–Pack k-point grid.[5]

According to previous reports, the cubic unit cells of $MAPbI_3$ and $FAPbI_3$, with lattice parameters of 6.3 Å and 6.316 Å, respectively, have been demonstrated to be the most stable perovskite phases at room temperature.[6,7] These lattice parameters are consistent with earlier experimental and theoretical studies.[8] The geometric optimization of the cubic unit cell was first carried out for both materials, and the resulting relaxed structures served as the basis for constructing the slab models used throughout this study. The slab models were generated by cleaving the optimized unit cells along the (001) plane for both $MAPbI_3$ and $FAPbI_3$, which has been reported as one of the most stable surfaces.[6,7] The unit cell optimization was performed using a 3 × 3 × 3 k-point grid, together with a 60 Ry cutoff energy for the wave function and 540 Ry for the charge density, which were maintained throughout the calculations. All atoms were allowed to relax within the unit cell until the Hellmann–Feynman forces were reduced below the convergence threshold specified earlier.

A 2 × 2 × 2.5 surface slab model exposing MAI/FAI terminations was used to investigate the interaction between GA^+ cations and halide ions (Cl^-) that constitute the passivating salt on defective $MAPbI_3$ and $FAPbI_3$ perovskite surfaces. In these models, MA^+/FA^+ and iodine vacancies were created simultaneously. The MA^+/FA^+ organic molecules and inorganic iodide ions were removed from the top surface to generate defective surfaces. A 15 Å vacuum layer was introduced along the z-direction to eliminate interactions between periodic images. A Γ-point (1

× 1 × 1) k-point grid was used for slab geometry optimization. Structural relaxation was performed using a fixed cell volume relaxation scheme, allowing only atomic positions to relax. Subsequently, GA^+ cations and halide anions were introduced near the MA^+/FA^+ and iodide vacancies, followed by structural re-optimization until all forces were less than 0.005 Ry/Å

To ensure that the adopted slab geometry and vacuum thickness do not introduce spurious electrostatic interactions between periodic images, the planar-averaged electrostatic potential along the surface normal (z-direction) was computed for both $MAPbI_3$ and $FAPbI_3$ systems with and without dipole correction under dark and illumination conditions. The electrostatic potential profiles show negligible differences, particularly in the vacuum region, indicating minimal spurious electrostatic interactions between periodic slabs (Figs. S15-S17). In addition, total SCF energies were compared for pristine, illuminated, and O_2-adsorbed systems (Table S1). For pristine slabs, the energies changed from $MAPbI_3$: −24736.339 Ry (without correction) to −24736.332 Ry (with correction), $FAPbI_3$: −25060.810 Ry (without correction) to −25060.806 Ry (with correction). Similar negligible variations were observed for illuminated and oxygen-adsorbed systems, with all energy differences remaining in the order of a few meV and relative deviations below 1% in most cases. These results confirm that dipole correction has a negligible effect on both electrostatic potential and total energy. Therefore, dipole correction was not included in subsequent calculations.

To evaluate the effects of water, oxygen, and passivating salt on the electronic properties, the density of states (DOS) and projected density of states (PDOS) were calculated using 3 × 3 × 1 and 6 × 6 × 1 k-point grids for self-consistent and non-self-consistent electronic structure calculations, respectively. The adsorption energy was also calculated to compare the relative interaction strengths of the passivating salts. Furthermore, to analyze the individual roles of cations and anions on electronic properties and stability, MA^+/FA^+ and iodide vacancies were created separately. The GA^+ cations and halide ions were then introduced near these vacancies, and the structures were re-optimized using the same energy cutoffs for the wave function and charge density.

Additionally, the same model was employed to study the interaction of water molecules and oxygen with $MAPbI_3$ and $FAPbI_3$ surfaces, as well as $MAPbI_3$ and $FAPbI_3$ surfaces treated with GACl passivation. Bulk-like conditions were maintained for the bottom layers, while the structures

were re-optimized until the forces converged to 0.005 Ry/Bohr, with the same energy parameters maintained.

Furthermore, the Nudged Elastic Band (NEB) method was employed to calculate the activation energy barrier between two energetically stable states. These states were obtained by removing iodine ions from the perfect crystal structures of $MAPbI_3$ and $FAPbI_3$, as well as from the structures passivated with GA^+ and Cl^-. A total of 10 images, including the two endpoints, were used to discretize the reaction path. The activation energy was determined from the difference between the maximum and minimum energy along the calculated images. During the NEB calculations, the self-consistency energy convergence criterion was set to 10^{-5} eV between two consecutive steps, and the atomic force threshold was set to 0.5 eV/Å.[9]

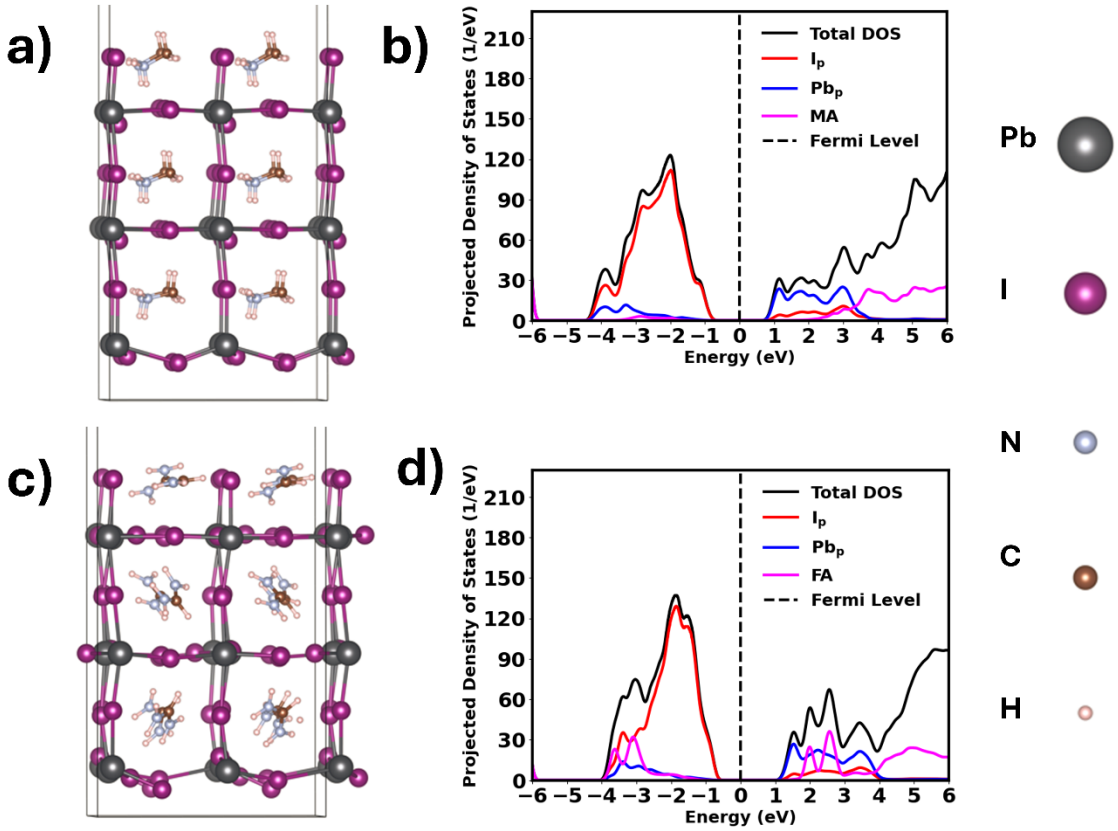

Figure S1: Pristine structures and projected density of states (PDOS) of $MAPbI_3$ and $FAPbI_3$. (a) Optimized slab model of pristine $MAPbI_3$ (001) surface; (b) corresponding PDOS showing contributions from I p, Pb p, and MA states with the Fermi level indicated by the dashed line. (c) Optimized slab model of pristine $FAPbI_3$ (001) surface; (d) corresponding PDOS showing contributions from I p, Pb p, and FA states.

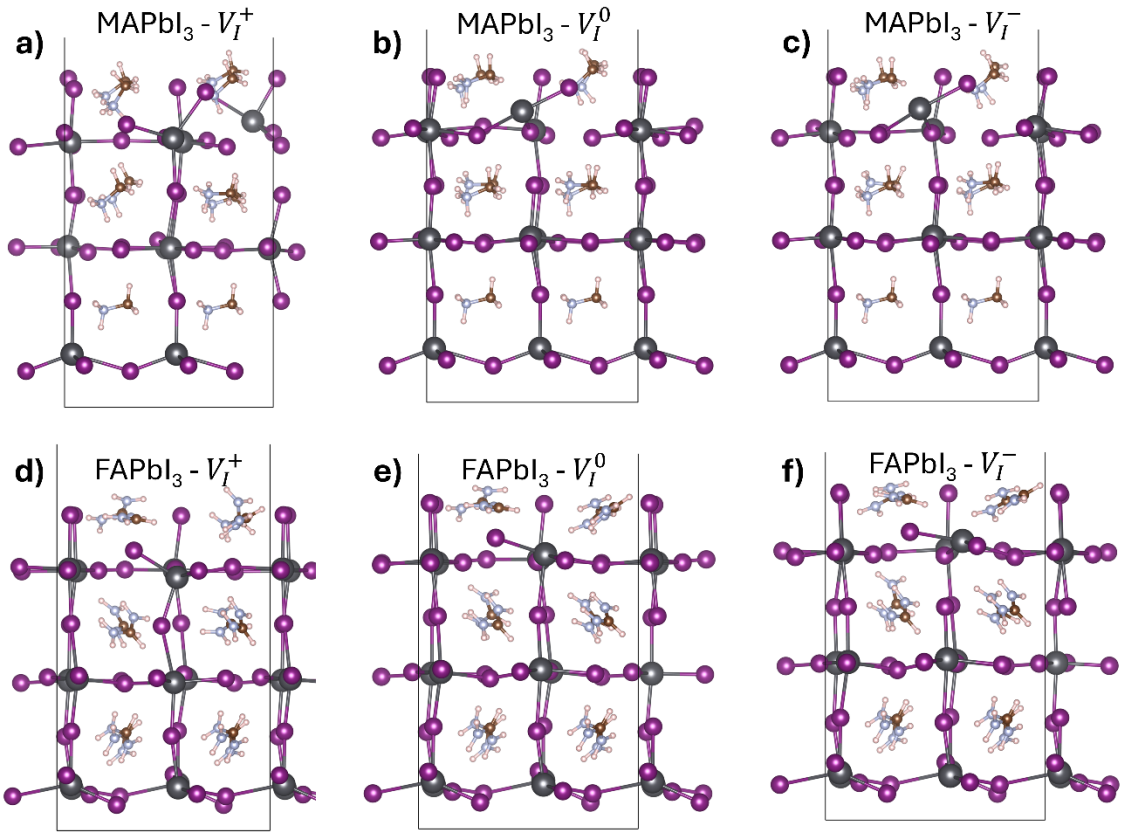

Figure S2: Optimized structures of $MAPbI_3$ and $FAPbI_3$ (001) surfaces containing an iodide vacancy (V_I) with different charge states, calculated using slab models with fixed bottom layers. (a–c) $FAPbI_3$ surfaces with V_I in charge states (a) +1, (b) 0, and (c) −1. (d–f) $FAPbI_3$ surfaces with V_I in charge states (d) +1, (e) 0, and (f) −1. The fixed bottom layers mimic bulk-like constraints, while the remaining atoms were fully relaxed during structural optimization. Color code: Pb (gray), I (purple), N (light blue), C (brown), and H (light pink).

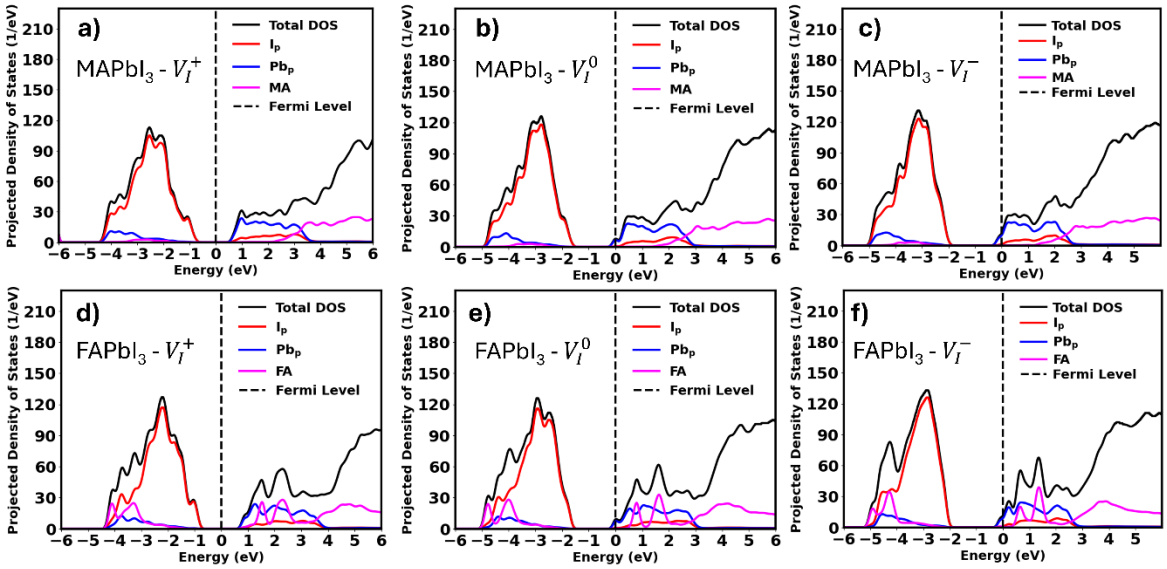

Figure S3: Projected density of states (PDOS) of $MAPbI_3$ and $FAPbI_3$ (001) surfaces containing iodide vacancies (V_I) with different charge states, calculated using slab models with fixed bottom layers (corresponding to the structures in Figure S2). (a–c) $MAPbI_3$ surfaces with V_I in charge states (a) +1, (b) 0, and (c) −1. (d–f) $FAPbI_3$ surfaces with V_I in charge states (d) +1, (e) 0, and (f) −1. The total density of states and orbital-projected contributions are shown, with the Fermi level indicated by the vertical dashed line. Contributions from I p, Pb p, and organic A-site cations (MA/FA) are highlighted.

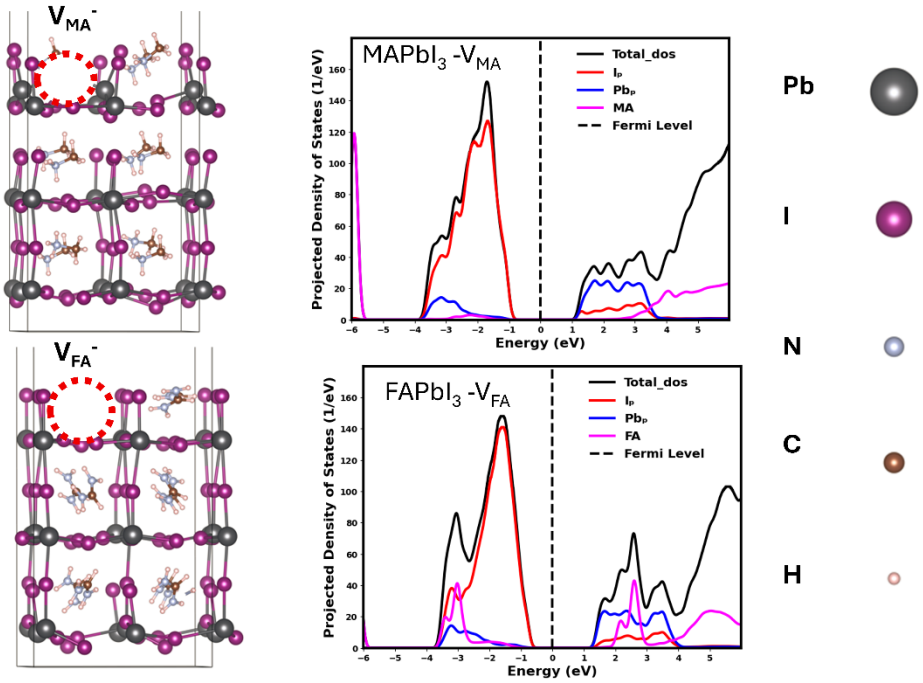

Figure S4: Optimized structures and projected density of states (PDOS) of $MAPbI_3$ and $FAPbI_3$ (001) surfaces containing isolated A-site vacancies. (Top) $MAPbI_3$ surface with a methylammonium vacancy (V_{MA}^{-}) and its corresponding PDOS. (Bottom) $FAPbI_3$surface with a formamidinium vacancy (V_{FA}^{-}) and its corresponding PDOS. The structural models highlight the vacancy sites, while the PDOS plots show the total density of states and orbital-projected contributions, with the Fermi level indicated by the vertical dashed line. Contributions from I p, Pb p, and organic A-site cations (MA/FA) are shown.

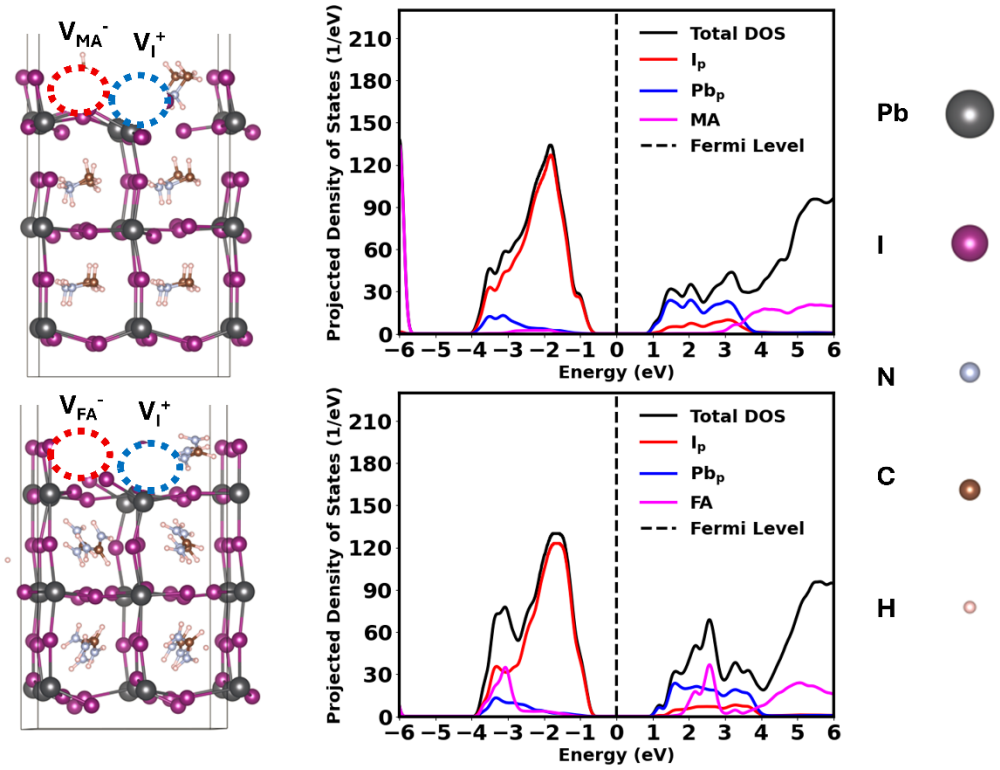

Figure S5: Optimized structures and projected density of states (PDOS) of $MAPbI_3$ and $FAPbI_3$(001) surfaces containing coexisting A-site and iodide vacancies. (Top) $MAPbI_3$ surface with a methylammonium vacancy (V_{MA}^{-}) and a positively charged iodide vacancy (V_I^{+}), together with the corresponding PDOS. (Bottom) $FAPbI_3$ surface with a formamidinium vacancy (V_{FA}^{-}) and a positively charged iodide vacancy (V_I^{+}), together with the corresponding PDOS. The structural models highlight the vacancy sites, while the PDOS plots present the total and orbital-projected density of states with the Fermi level indicated by the vertical dashed line. Contributions from I p, Pb p, and organic A-site cations (MA/FA) are shown.

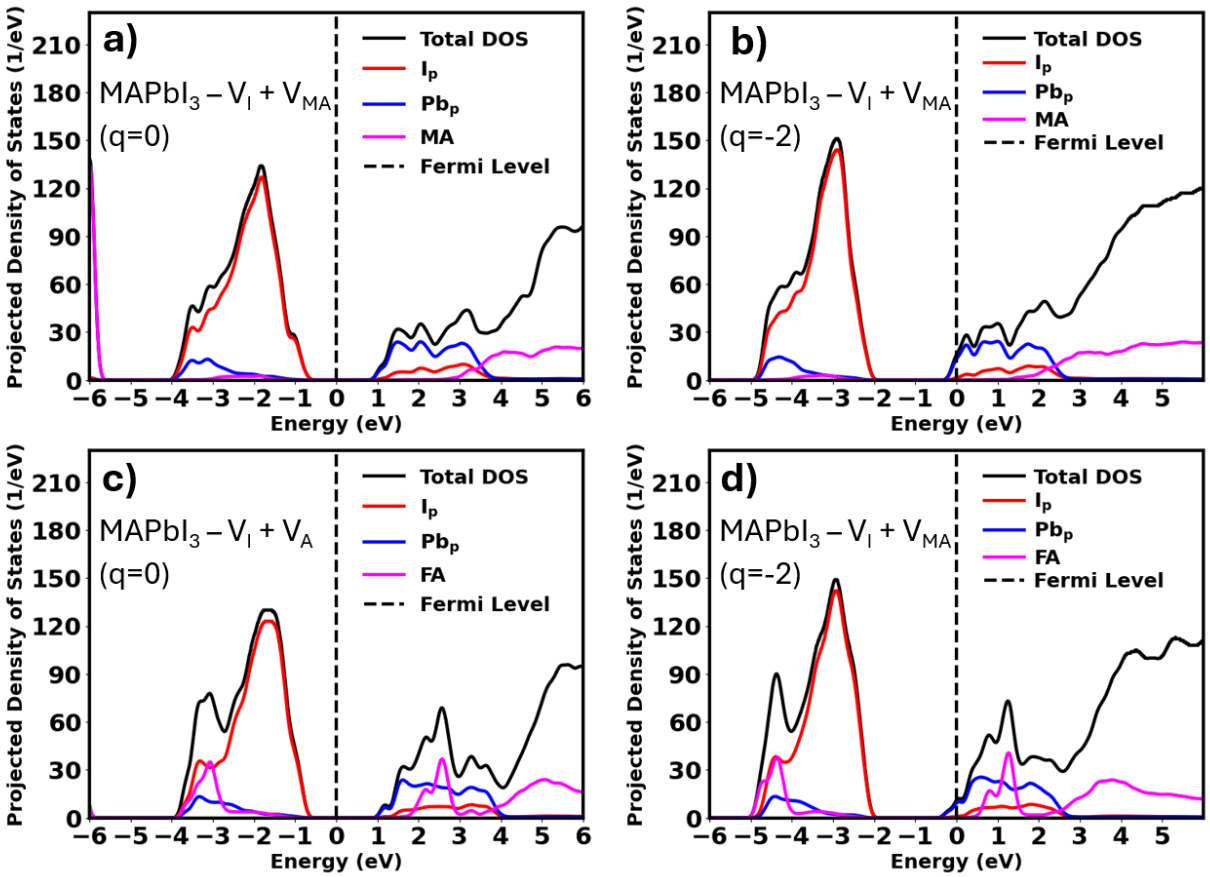

Figure S6: Projected density of states (PDOS) of $MAPbI_3$ and $FAPbI_3$ (001) surfaces containing coexisting iodide and A-site vacancies under neutral and illuminated conditions. (a) $MAPbI_3$ with V_I and V_{MA} under neutral conditions (q = 0); (b) $MAPbI_3$ with V_I and V_{MA} under excess-electron conditions (q = −2); (c) $FAPbI_3$ with V_I and V_{FA} under neutral conditions (q = 0); and (d) $FAPbI_3$with V_I and V_{FA} under excess-electron conditions (q = −2). The total and orbital-projected density of states are shown with the Fermi level indicated by the vertical dashed line.

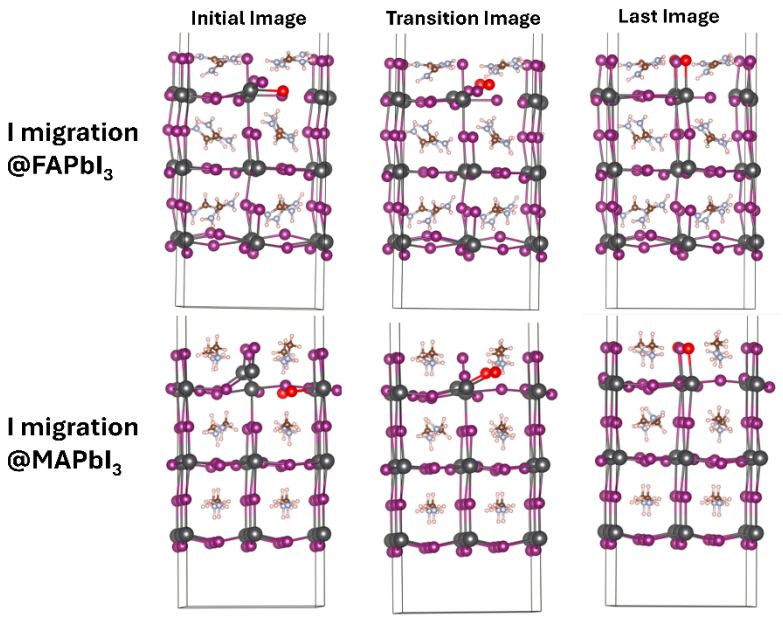

Figure S7. Initial, transition, and final configurations from nudged elastic band (NEB) calculations of iodide migration on pristine perovskite surfaces. (Top) Iodide migration pathways on $FAPbI_3$(001). (Bottom) Iodide migration pathways on $MAPbI_3$ (001). Atomic relaxations illustrate the diffusion of iodide ions between adjacent lattice sites during migration.

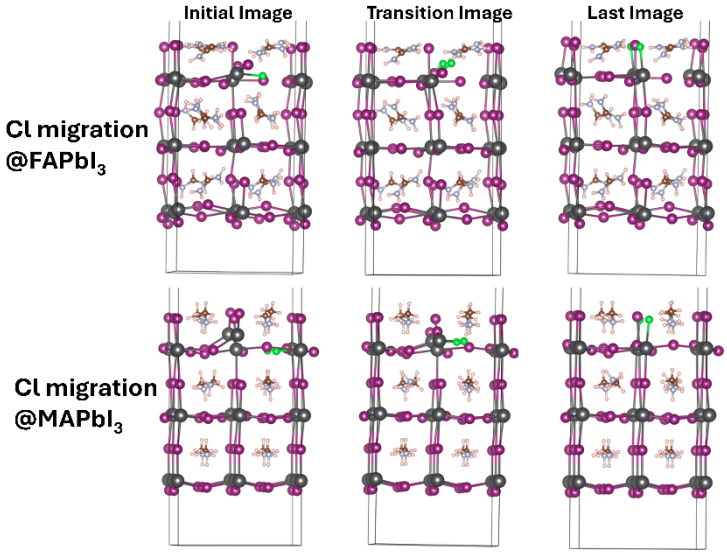

Figure S8. Initial, transition, and final configurations from NEB calculations of chloride migration on pristine perovskite surfaces. (Top) Chloride migration pathways on $FAPbI_3$ (001). (Bottom) Chloride migration pathways on $MAPbI_3$ (001). Structural evolution highlights the migration mechanism of Cl ions across surface lattice sites.

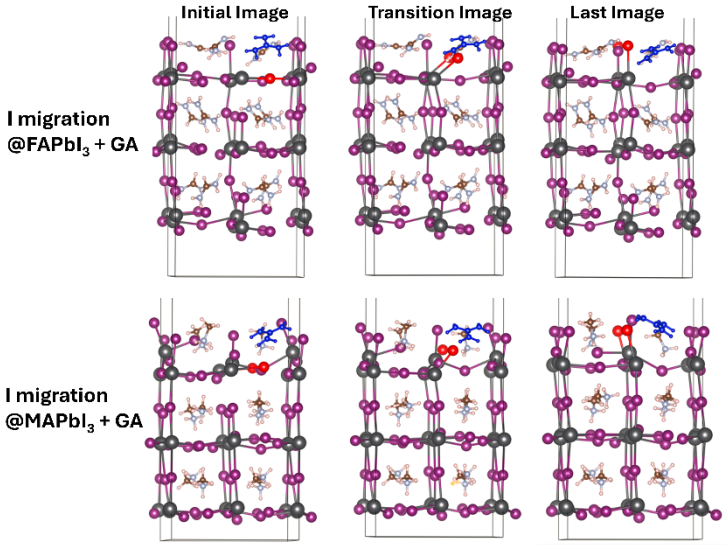

Figure S9. Initial, transition, and final configurations from NEB calculations of iodide migration on GA-passivated perovskite surfaces. (Top) Iodide migration pathways on GA-passivated $FAPbI_3$ (001). (Bottom) Iodide migration pathways on GA-passivated $MAPbI_3$ (001). The presence of GA modifies local lattice environments and alters iodide diffusion pathways.

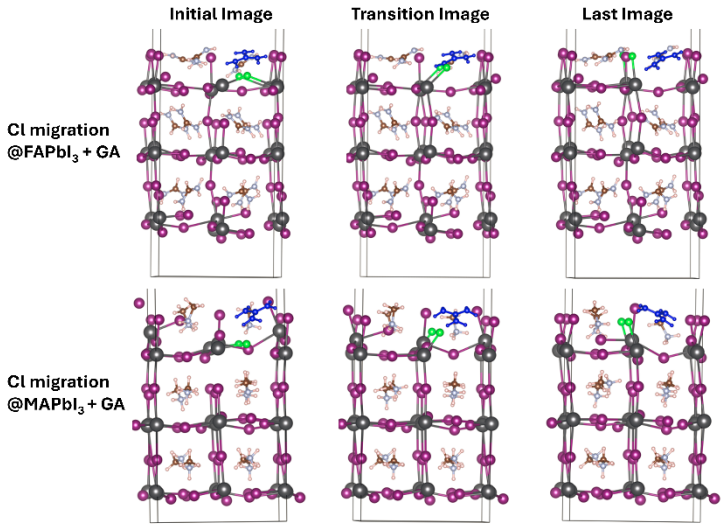

Figure S10. Initial, transition, and final configurations from NEB calculations of chloride migration on GA-passivated perovskite surfaces. (Top) Chloride migration pathways on GA-passivated $FAPbI_3$ (001). (Bottom) Chloride migration pathways on GA-passivated $MAPbI_3$ (001). GA passivation modifies halide coordination environments and influences Cl migration behavior.

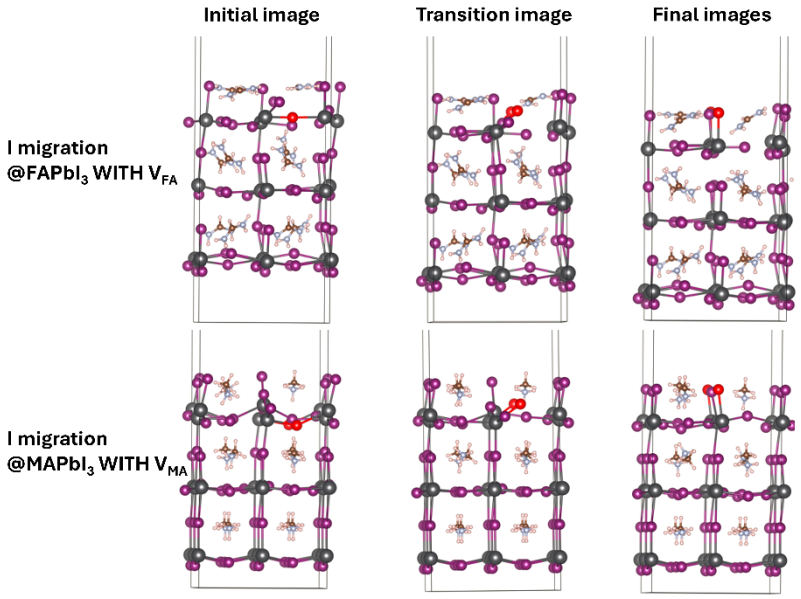

Figure S11. Initial, transition, and final configurations from NEB calculations of iodide migration on perovskite surfaces containing A-site vacancies. (Top) Iodide migration pathways on $FAPbI_3$ (001) with a V_{FA} vacancy. (Bottom) Iodide migration pathways on $MAPbI_3$ (001) with a V_{MA} vacancy. Vacancy-assisted diffusion pathways and associated lattice relaxations are illustrated.

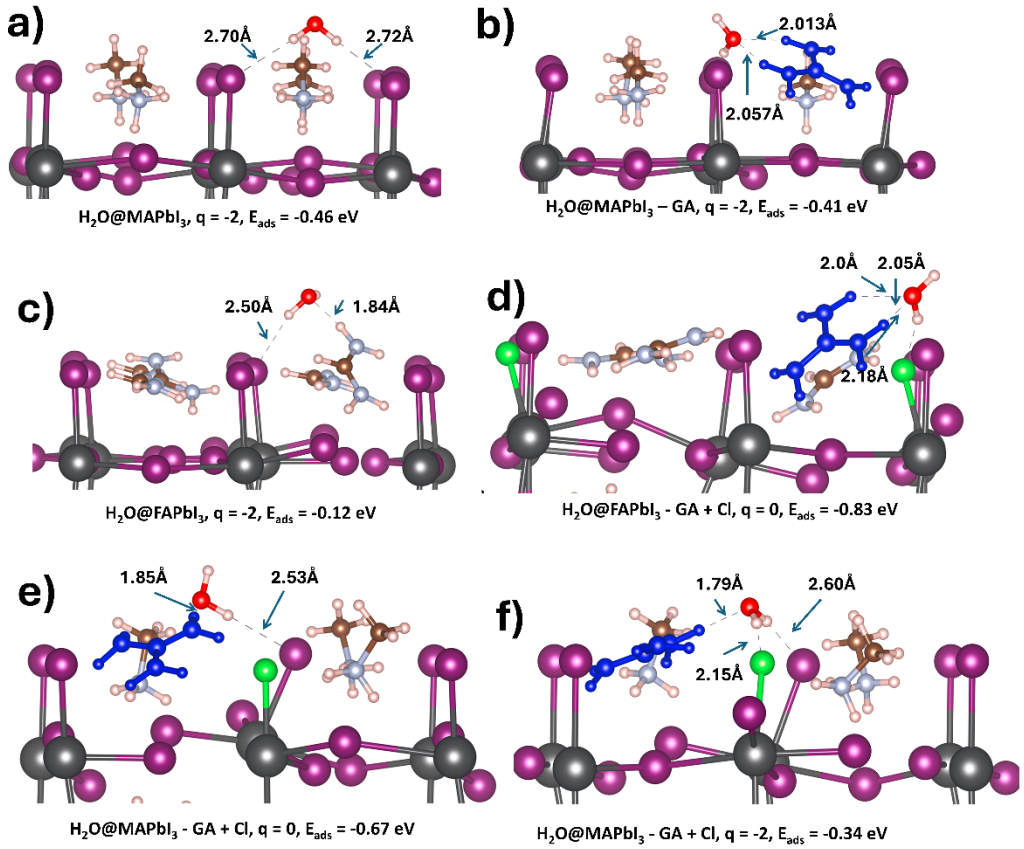

Figure S12. Optimized configurations of H_2O adsorption on $MAPbI_3$ and $FAPbI_3$ (001) surfaces with and without GA-based passivation under neutral and excess-electron conditions. (a) H_2O adsorption on pristine $MAPbI_3$ (q = −2); (b) GA-passivated $MAPbI_3$ (q = −2); (c) pristine $FAPbI_3$ (q = −2); (d) GACl-passivated $FAPbI_3$ (q = 0); (e) GACl-passivated $MAPbI_3$ (q = 0); and (f) GACl-passivated $MAPbI_3$ (q = −2). Selected intermolecular distances (Å) indicating hydrogen-bond interactions are labeled. The corresponding adsorption energies (E_{ads}) are shown in each panel.

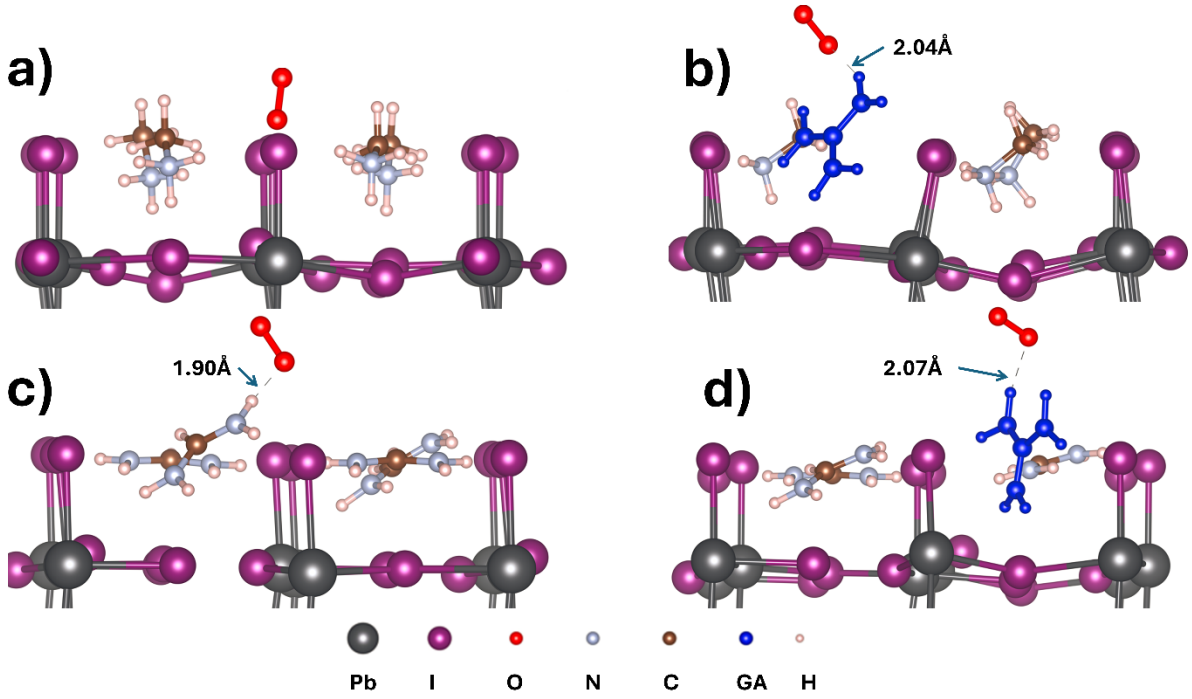

Figure S13. Optimized configurations of O_2 adsorption on perovskite (001) surfaces under dark (neutral) conditions. (a) O_2 adsorption on pristine $MAPbI_3$; (b) O_2 adsorption on GA-passivated $MAPbI_3$; (c) O_2 adsorption on pristine $FAPbI_3$; and (d) O_2 adsorption on GA-passivated $FAPbI_3$. Selected intermolecular distances (Å) indicate weak physisorption interactions between O_2 molecules and surface species.

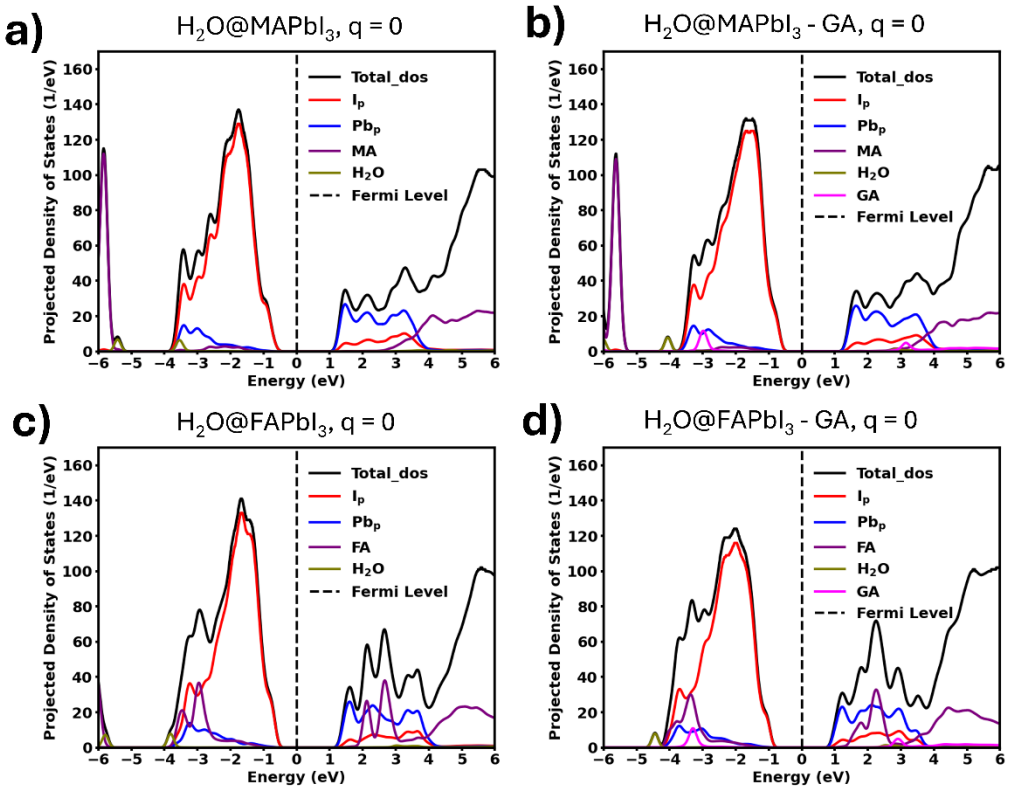

Figure S14. Projected density of states (PDOS) of H_2O-adsorbed perovskite (001) surfaces under neutral conditions (q = 0). (a) H_2O adsorption on pristine $MAPbI_3$; (b) H_2O adsorption on GA-passivated $MAPbI_3$; (c) H_2O adsorption on pristine $FAPbI_3$; and (d) H_2O adsorption on GA-passivated $FAPbI_3$. The total and orbital-projected density of states are shown with the Fermi level indicated by the vertical dashed line. Contributions from I p, Pb p, organic A-site cations (MA/FA), H_2O, and GA are highlighted.

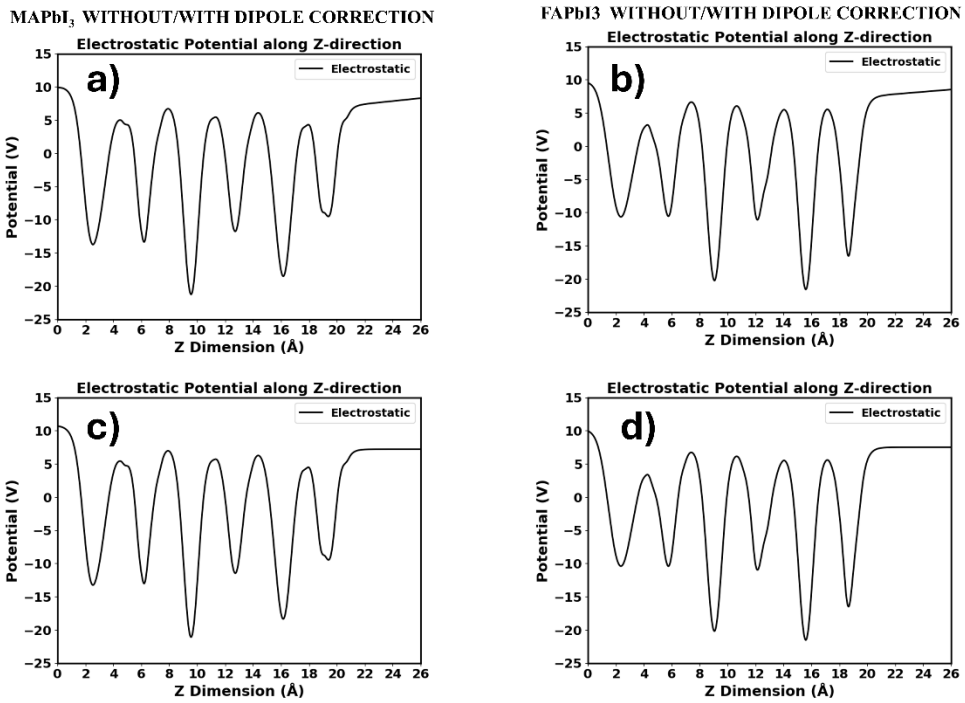

Figure S15. Planar-averaged electrostatic potential along the surface normal (z-direction) for (a) $MAPbI_3$ and (b) $FAPbI_3$ surfaces without dipole correction, and for (c) $MAPbI_3$ and (d) $FAPbI_3$ surfaces with dipole correction, calculated under neutral (dark) conditions.

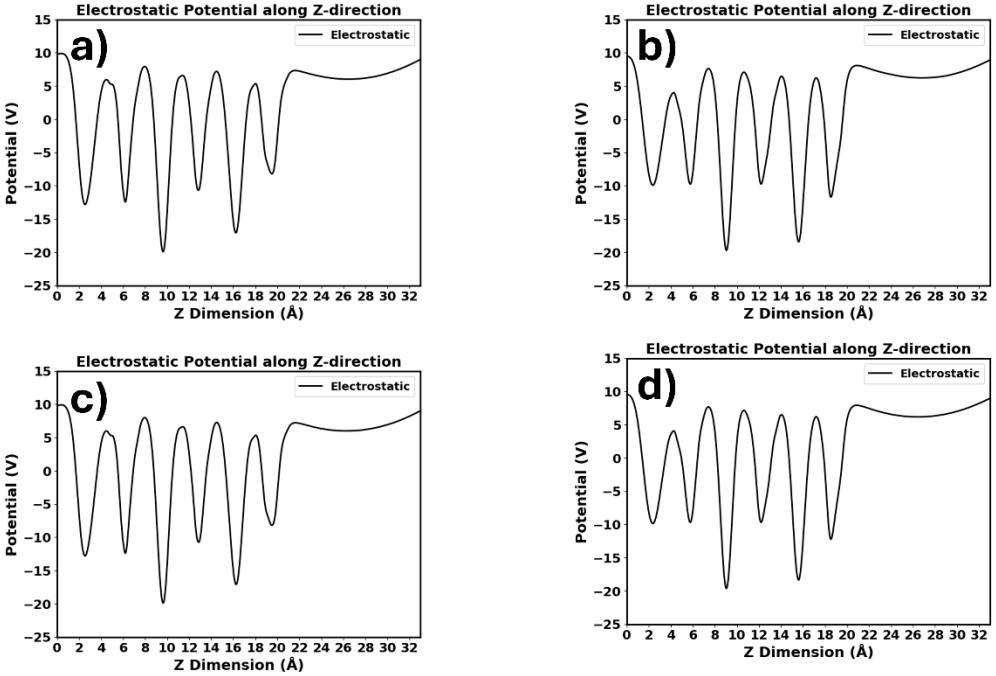

Figure S16. Planar-averaged electrostatic potential along the surface normal (z-direction) for (a) $MAPbI_3$ and (b) $FAPbI_3$ surfaces without dipole correction, and for (c) $MAPbI_3$ and (d) $FAPbI_3$ surfaces with dipole correction, calculated under illumination conditions.

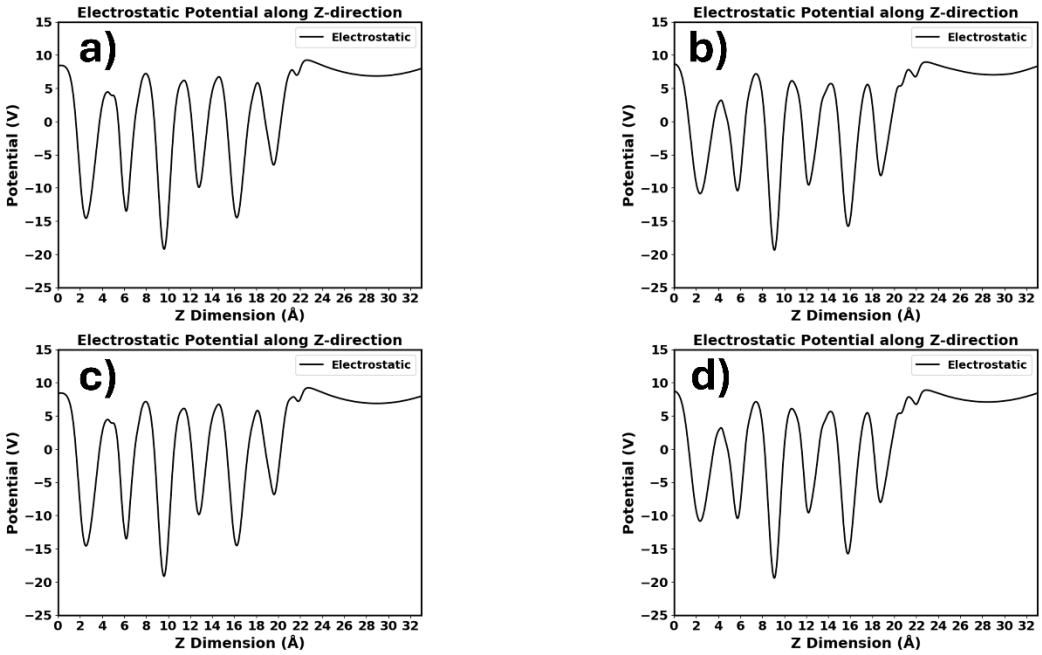

Figure S17. Planar-averaged electrostatic potential along the surface normal (z-direction) for (a) $MAPbI_3$ with H_2O and (b) $FAPbI_3$ with H_2O surfaces without dipole correction, and for (c) $MAPbI_3$ with H_2O and (d) $FAPbI_3$ with H_2O surfaces with dipole correction, calculated under illumination conditions.

Table S1. Self-consistent field (SCF) energies of $MAPbI_3$ and $FAPbI_3$ (001) slab models calculated with and without dipole correction under dark conditions, excess-electron (illumination) conditions ($q = -2$), and O_2 adsorption under illumination. The percentage error corresponds to the relative difference between the energies obtained from the two calculations.

System	Condition	SCF Energy without Dipole (Ry)	SCF Energy with Dipole (Ry)	Error (%)
$MAPbI_3$	Dark	−24736.339	−24736.332	0.621
$FAPbI_3$	Dark	−25060.806	−25060.810	0.372
$MAPbI_3$	Illumination	-24736.184	-24736.185	0.087
$FAPbI_3$	Illumination	-25060.653	-25060.655	0.178
$MAPbI_3$+O_2	Illumination	-24819.384	-24819.422	3.780
$FAPbI_3$+ O_2	Illumination	-25143.778	-25143.778	0.055

Table S2. Bader charge analysis of atoms adjacent to surface iodide vacancies (V_I) in $MAPbI_3$ and $FAPbI_3$ (001) surfaces. Δq represents the change in Bader charge relative to the pristine surface. I_{eq} and I_{ap} denote the neighboring equatorial and apical (vertical) iodine atoms, respectively.

system	Vacancy type	Nearby atom	Perfect system	Defective charge	Δq (e)
$MAPbI_3$	V^-	Pb	13.073	13.297	0.224
$MAPbI_3$	V^-	Pb	13.073	13.452	0.379
$MAPbI_3$	V^-	I_{eq}	7.553	7.573	0.020
$MAPbI_3$	V^-	I_{eq}	7.553	7.616	0.063
$MAPbI_3$	V^+	Pb	13.073	13.081	0.008
$MAPbI_3$	V^+	Pb	13.073	13.060	-0.013
$MAPbI_3$	V^+	I_{eq}	7.553	7.533	-0.021
$MAPbI_3$	V^+	I_{ap}	7.602	7.542	-0.060
$MAPbI_3$	V^0	Pb	13.073	13.104	0.031
$MAPbI_3$	V^0	Pb	13.073	13.103	0.030
$MAPbI_3$	V^0	I_{eq}	7.553	7.538	-0.016
$MAPbI_3$	V^0	I_{ap}	7.560	7.570	0.010
$FAPbI_3$	V^-	Pb	13.089	13.378	0.289
$FAPbI_3$	V^-	Pb	13.072	13.638	0.565
$FAPbI_3$	V^-	I_{eq}	7.530	7.614	0.084
$FAPbI_3$	V^-	I_{eq}	7.560	7.473	-0.087
$FAPbI_3$	V^+	Pb	13.089	13.093	0.004
$FAPbI_3$	V^+	Pb	13.072	13.091	0.018
$FAPbI_3$	V^+	I_{eq}	7.530	7.581	0.052
$FAPbI_3$	V^+	I_{eq}	7.524	7.518	-0.006
$FAPbI_3$	V^0	Pb	13.089	13.107	0.018
$FAPbI_3$	V^0	Pb	13.072	13.493	0.420
$FAPbI_3$	V^0	I_{eq}	7.560	7.516	-0.044
$FAPbI_3$	V^0	I_{eq}	7.530	7.593	0.063

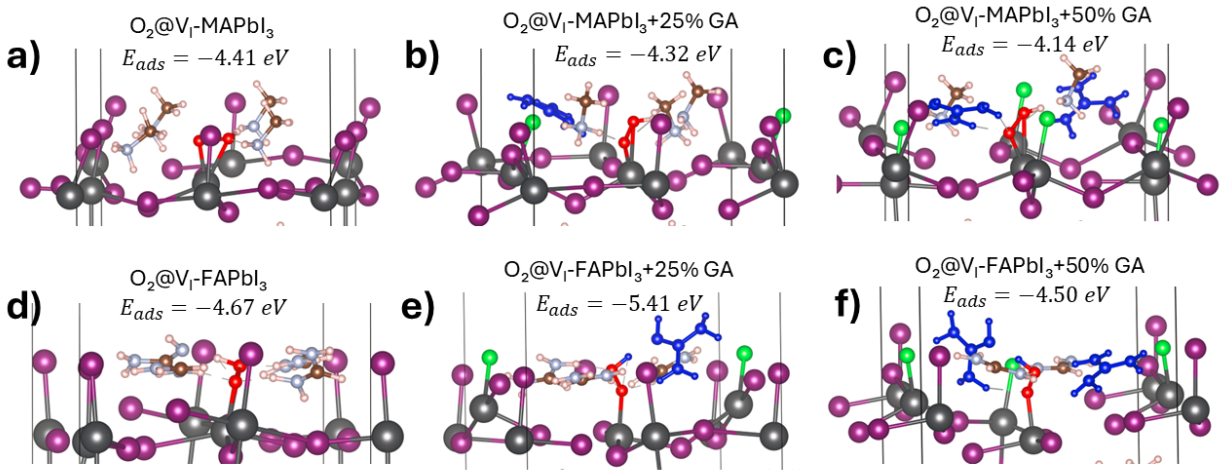

Figure S18. Optimized structures of O_2 adsorbed at surface iodide-vacancy sites under excess-electron conditions (q = −1) for (a) pristine $MAPbI_3$, (b) 25% GA-passivated $MAPbI_3$, (c) 50% GA-passivated $MAPbI_3$, (d) pristine $FAPbI_3$, (e) 25% GA-passivated $FAPbI_3$, and (f) 50% GA-passivated $FAPbI_3$. The corresponding adsorption energies (E_{ads}) are indicated in each panel.

References

1 P. Giannozzi, O. Andreussi, T. Brumme, O. Bunau, M. B. Nardelli, M. Calandra, R. Car, C. Cavazzoni, D. Ceresoli, M. Cococcioni and others, Advanced capabilities for materials modelling with Quantum ESPRESSO. (arXiv:1709.10010v1 [cond-mat.mtrl-sci]), *Journal of Physics: Condensed Matter*, 2017, **29**, 465901.

2 P. Giannozzi, S. Baroni, N. Bonini, M. Calandra, R. Car, C. Cavazzoni, D. Ceresoli, G. L. Chiarotti, M. Cococcioni, I. Dabo, A. Dal Corso, S. De Gironcoli, S. Fabris, G. Fratesi, R. Gebauer, U. Gerstmann, C. Gougoussis, A. Kokalj, M. Lazzeri, L. Martin-Samos, N. Marzari, F. Mauri, R. Mazzarello, S. Paolini, A. Pasquarello, L. Paulatto, C. Sbraccia, S. Scandolo, G. Sclauzero, A. P. Seitsonen, A. Smogunov, P. Umari and R. M. Wentzcovitch, QUANTUM ESPRESSO: A modular and open-source software project for quantum simulations of materials, *Journal of Physics Condensed Matter*, DOI:10.1088/0953-8984/21/39/395502.

3 H. M. Ghaithan, Z. A. Alahmed, S. M. H. Qaid and A. S. Aldwayyan, Density Functional Theory Analysis of Structural, Electronic, and Optical Properties of Mixed-Halide Orthorhombic Inorganic Perovskites, *ACS Omega*, 2021, **6**, 30752–30761.

4 S. Grimme, Accurate description of van der Waals complexes by density functional theory including empirical corrections, *J. Comput. Chem.*, 2004, **25**, 1463–1473.

5 J. D. Pack and H. J. Monkhorst, *'Special points for Brillonln-zone integrations'-a reply**, 1977.

6 F. F. Targhi, Y. S. Jalili and F. Kanjouri, MAPbI3 and FAPbI3 perovskites as solar cells: Case study on structural, electrical and optical properties, *Results Phys.*, 2018, **10**, 616–627.

7 C. Jiang, Y. Wang, R. Zhou, H. Wang and Q. Chen, Air molecules in XPbI3 (X=MA, FA, Cs) perovskite: A degradation mechanism based on first-principles calculations, *J. Appl. Phys.*, DOI:10.1063/1.5037005.

8 A. Bonadio, F. P. Sabino, A. L. M. Freitas, M. R. Felez, G. M. Dalpian and J. A. Souza, Comparing the Cubic and Tetragonal Phases of MAPbI3 at Room Temperature, *Inorg. Chem.*, 2023, **62**, 7533–7544.

9 G. Henkelman, B. P. Uberuaga and H. Jónsson, Climbing image nudged elastic band method for finding saddle points and minimum energy paths, *Journal of Chemical Physics*, 2000, **113**, 9901–9904.